Journal Pre-proofs

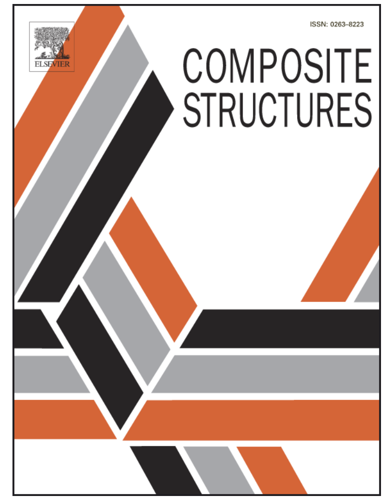

High strain rate characterisation of intralaminar fracture toughness of GFRPs for longitudinal tension and compression failure

Giuseppe Catalanotti, P. Kuhn, J. Xavier, H. Koerber

PII: S0263-8223(19)34395-8
DOI: https://doi.org/10.1016/j.compstruct.2020.112068
Reference: COST 112068

To appear in: *Composite Structures*

Received Date: 18 November 2019
Accepted Date: 14 February 2020

Please cite this article as: Catalanotti, G., Kuhn, P., Xavier, J., Koerber, H., High strain rate characterisation of intralaminar fracture toughness of GFRPs for longitudinal tension and compression failure, *Composite Structures* (2020), doi: https://doi.org/10.1016/j.compstruct.2020.112068

High strain rate characterisation of intralaminar fracture toughness of GFRPs for longitudinal tension and compression failure

Giuseppe Catalanotti[a,*], P. Kuhn[b], J. Xavier[c], H. Koerber[b]

[a] *Advanced Composites Research Group (ACRG), School of Mechanical and Aerospace Engineering, Queen's University Belfast, Belfast BT9 5AH, UK*
[b] *Technical University of Munich, Department of Mechanical Engineering, Chair of Carbon Composites, Boltzmannstraße 15, 85748 Garching, Germany*
[c] *Department of Mechanical and Industrial Engineering, UNIDEMI, Faculty of Sciences and Technology, NOVA University of Lisbon, 2928-516 Caparica, Portugal*

Abstract

The elastic parameters, strengths, and intralaminar fracture toughness are determined for an E-Glass polymer composite material system, statically and at high strain rate, adapting methodologies previously developed by the authors for different carbon composites. Dynamic experiments are conducted using tension and compression Split-Hopkinson Bars (SHBs). A unique set of experimental parameters is obtained, and reported together with the experimental set-up, in order to ensure reproducibility. While in-plane elastic and strength properties were obtained by testing one specimen geometry, intralaminar fracture properties required the testing of different sized notched specimens with scaled geometries. This allowed the use of the size-effect method for the determination of the dynamic R-curve. When comparing these results with those previously obtained for a carbon/epoxy material system, it is observed that the dynamic fracture toughness exhibits a much more significant increase in both tension and compression. The obtained results permit the identification of the softening law at different strain rates, allowing its use in any analytical or numerical strength predictive method.

Keywords: Glass fibre reinforced plastics (GFRPs), Dynamic characterisation, Size-effect, Intralaminar R-curve

1. Introduction

Fibre reinforced plastics are strain rate dependent and, even if no standard test methods exist, several works (summarised in [1–3]) have been conducted in order to measure their strain rate dependency. Generally, there is a consensus for their elastic and strength properties, but not for their fracture properties.

*Corresponding author
Email address: G.Catalanotti@qub.ac.uk (Giuseppe Catalanotti)

The development of test methods to measure the dynamic interlaminar fracture toughness has been motivated by the necessity of characterising the development and propagation of delamination induced by low-velocity impact. The works performed so far have been inconclusive [4]; there is no agreement on the optimal testing procedure, and no agreement on the trend that the interlaminar fracture toughness should exhibit with strain rate.

Little attention has been given to the intralaminar fracture toughness [5–8] and, to the authors' best knowledge, this has been limited to carbon fibre reinforced plastics (CFRPs).

However, there are numerous applications where glass fibre reinforced plastics (GFRPs) could experience dynamic loadings, including in the automotive, maritime, wind turbine, tanks, and pipe industries. The lack of knowledge on the dynamic fracture toughness of such materials inhibits their modelling. Therefore, its experimental determination is of crucial importance, but has so far been neglected by the scientific community.

Here, an experimental methodology is proposed for the dynamic characterisation of an E-Glass/epoxy composite laminate. The determination of the salient properties necessary for the identification of the softening law (stiffness, strength, and intralaminar fracture toughness) is made by adapting the methodologies proposed by the authors in previous studies conducted on CFRPs.

The use of the size-effect method [6, 7, 9–13] allowed the intralaminar fracture toughness and R-curve to be measured in both tension (fibre fracture) and compression (development of a kink-band), and a significant strain-rate dependency has been noticed in both cases. This is different from what was obtained by Kuhn et al. [6, 7] who, when testing IM7/8552, observed a significant increase of the fracture toughness only in compression but not in tension, where a more modest increase was reported.

2. Materials and methods

2.1. Specimen manufacturing

Panels were manufactured by resin transfer moulding (RTM) using Saertex non-crimp fabric (NCF) E-Glass (X-E-PB-627g/m^2) and Sika epoxy resin (CR80, hardener: CH80-2). The resin was degassed for 10 min at 1 bar vacuum, and later injected by using a pressure pot. The pressure gradient in the RTM tool was initially set to 2 bar, and increased up to 6.5 bar when the outlet was pinched-off during the injection process.

Cross ply panels having layup of $[90/0]_{5s}$, with a nominal thickness of 4 mm and a fibre volume content (FVC) of 58% (determined through the burn-off test), were manufactured for the compression specimens. For tension, two layups were manufactured, $[90/0]_{2s}$, and $[\pm 45]_{2s}$, both with a nominal thickness of 1.5 mm and a FVC of 59% and 54%, respectively.

Several tests were considered in this study at both quasi-static (QS) and high strain rate (HR) regimes and using unnotched and notched specimens. Specimens were cut using a water-cooled diamond saw and additionally grinded in order to ensure the perfect flatness and parallelism of the end surfaces. Notches were machined using 1 mm diameter milling bits, and consequently the notch tip radius was 0.5 mm. Tab. 1 reports the geometries and layups for each specimen typology, together with the labels that will be used throughout the text.

Table 1: Investigated specimens.

specimen label	test method	layup	width [mm]	length [mm]	thickness [mm]	initial notch a_0 [mm]
UNC	unnotched compression	$[90/0]_{5s}$	15	10	4	–
UNT	unnotched tension	$[90/0]_{2s}$	20	8	1.5	–
UNTS	unnotched shear (tested in tension)	$[\pm 45]_{2s}$	20	8	1.5	–
DENC	double edge notched compression	$[90/0]_{5s}$	$2w$	$3w$	t	$0.5w$
DENC-A	" " " "	"	10	15	4	2.5
DENC-B	" " " "	"	15	22.5	4	3.75
DENC-C	" " " "	"	20	30	4	5
DENC-D	" " " "	"	25	37.5	4	6.25
DENT	double edge notched tension	$[90/0]_{2s}$	$2w$	$5w^*$	t	$0.6w$
DENT-A	" " " "	"	8	20	1.5	2.4
DENT-B	" " " "	"	12	30	1.5	3.6
DENT-C	" " " "	"	16	40	1.5	4.8

* This value refers to the free length of the specimen.

DENC and DENT specimens (unlike UNC, UNT, and UNTS) had different dimensions, to allow the calculation of the dynamic fracture toughness through the size-effect method [6, 7, 9, 10]. In these specimens, notches were machined by using a 1 mm diameter milling bit (Figs. 1 and 2).

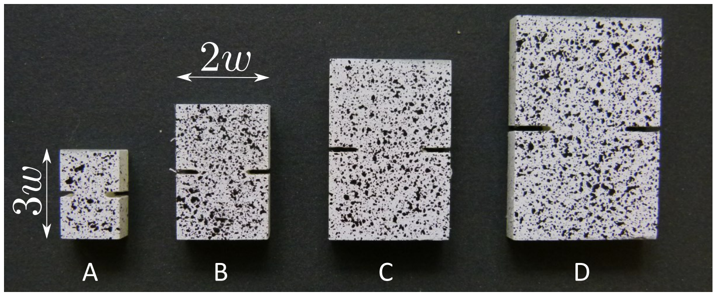

Figure 1: Machined and painted DENC specimens.

All tensile specimens (UNT, UNTS, DENT) were glued (using 3M Scotchweld DP 490) to slotted steel adaptors (visible in Fig. 2). The adapters had an outer thread in order to be mechanically connected to the loading device.

Finally, to enable the use of Digital Image Correlation (DIC), a black-on-white speckle pattern was applied to all specimens using a water-based spray paint (as shown in Fig. 1).

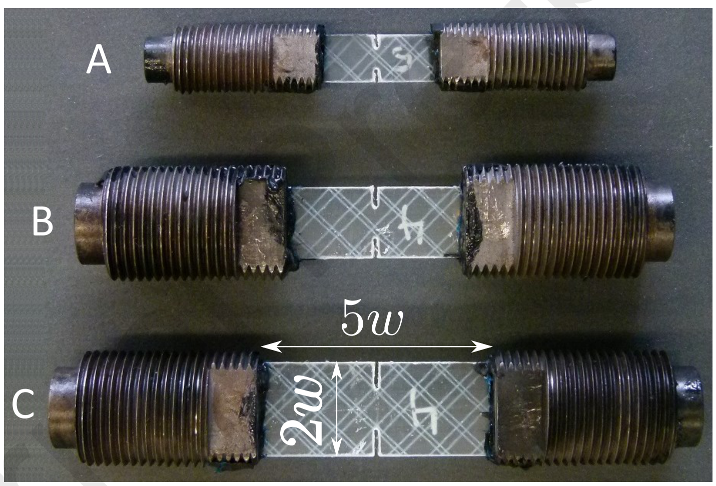

Figure 2: DENT specimen glued to steel adaptors.

2.2. Experimental set-up

2.2.1. Quasi-static

The quasi-static (QS) test were performed in a Hegewald & Peschke Inspect Table 100 universal testing machine. The speed of the cross head (Tab. 2) was chosen in function of the free length of the specimen, L, in order to provide the same strain rate (10^{-4} s^{-1}). A load cell of 100 kN was used.

Table 2: Crosshead displacement rate for HR compressive (left) and tensile (right) specimens.

Specimen	v_C [mm/min]
UNC	0.15
DENC-A	0.15
DENC-B	0.225
DENC-C	0.30
DENC-D	0.375

Specimen	v_C [mm/min]
UNT	0.5
UNTS	1.0
DENT-A	0.50
DENT-B	0.75
DENT-C	1.0

For the compression tests, a self alignment device (see [14]) was used, and a thin layer of molybdenum disulphide (MoS_2) was put at the loaded edge of the specimen in order to minimise the friction.

In addition, the DIC optical system GOM ARAMIS-4M was used in stereo configuration (two CCD cameras with a resolution of 1728×2352 pixel^2). Frame rate and shutter speed were carefully chosen in order to capture a sufficient number of images for each specimen in both tension (2 fps, 60 ms) and compression (1 fps, 50 ms).

2.2.2. Dynamic Compression

A split-Hopkinson pressure bar (SHPB) was used for the high rate (HR) compression tests (Fig. 3). The lengths of the steel bars were 0.8, 2.6, and 1.3 m for the striker-, incident-, and transmission-bar, respectively. The bars' diameters, d_b, are reported in Tab. 3. The strain gauges for the incident- and transmission-bar were located at 1.3 m and 0.3 m away from the bar-specimen interface. A Finite Element Model was used to find the optimal SHPB configuration and to ensure that the axial strain rate was the same for every specimen size (≈ 100 s-1). The diameter and thickness (d_{PS}, t_{PS}) of the copper pulse shapers, for the corresponding striker velocity, v_s, was determined using the Pulse Shaper Analysis (PSA) described in [15] (Tab. 3).

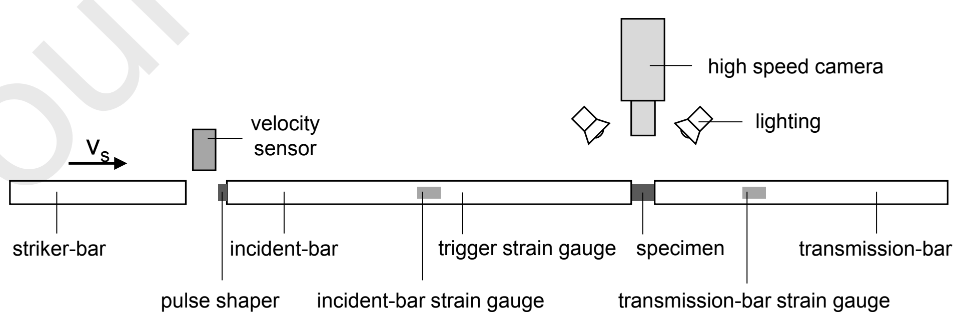

Figure 3: Photo-mechanical setup for dynamic compressive tests (after [6]).

Table 3: SHPB parameters.

Specimen	w [mm]	d_b [mm]	v_s [m/s]	d_{PS} [mm]	t_{PS} [mm]
UNC	5	16	7.4	8	1.5
DENC-A	5	16	7.1	6	1.5
DENC-B	7.5	18	8.2	8	2
DENC-C	10	18	9.7	10	2
DENC-D	12.5	25	10.7	10	2

2.2.3. Dynamic Tensile

The HR tensile tests were performed on a split-Hopkinson tension bar (SHTB) equipped with a U-shaped striker-bar [16] (Fig. 4). To achieve the same overall axial strain rate, the striker velocity, v_s, was different for each specimen (Tab. 4). The length of the striker-bar, l_s, was 1.0 m and 0.8 m, for the unnotched and notched specimens, respectively (Tab. 4). The titanium loading-, incident- and transmission-bars had a length of 2.15, 3 and 1.8 m, respectively. The bar diameters d_b of the incident- and transmission-bar were chosen in function of the specimen size (Tab. 4), while the loading bar's diameter was kept constant and equal to 20 mm. Strain gauges were located at 1.58 and 0.20 m away from the specimen/bar interface for the incident- and transmission-bar, respectively. In order to obtain a ramped-shaped incident wave [17, 18], layered rings of silicon rubber with a thickness of 2 mm, were used as pulse shapers.

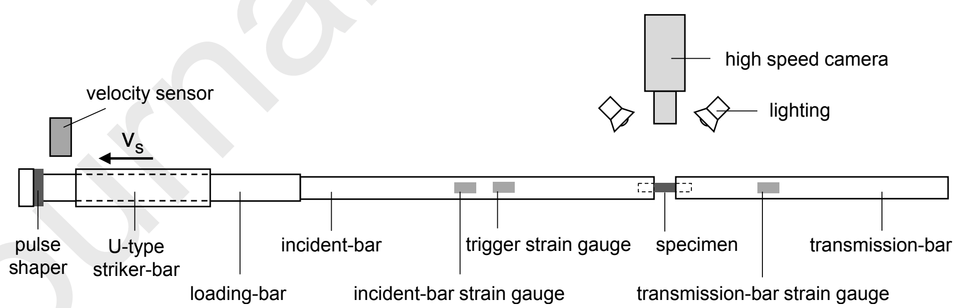

Figure 4: Photo-mechanical setup for dynamic tensile tests (after [7]).

Table 4: SHTB parameters.

Specimen	w	d_b	l_s	v_s
	[mm]	[mm]	[mm]	[m/s]
UNT	4	16	1000	6.7
UNTS	4	16	1000	4.7
DENT-A	4	16	800	5.1
DENT-B	6	25	800	7.6
DENT-C	8	25	800	9.9

Specimen deformation was monitored using a Photron FASTCAM SA-Z high speed camera (frame rate: 300,000 fps, resolution: 256 × 128 pixel^2). To enable a reliable synchronization of the data obtained from the bars' strain gauges and the optical measurement, the high speed camera was triggered automatically using an additional strain gauge, which was mounted on the incident-bar.

2.3. Data reduction methods

2.3.1. Stresses and strains

For the QS tests, the nominal value of the longitudinal stress, σ_s, was trivially calculated as $\sigma_s = F/A_s$ were F is the load and A_s is the specimen cross sectional area equal to $A_s = 2wt$ (see Tab. 1).

For the HR loading the longitudinal stress was calculated resorting to the classic split-Hopkinson pressure bar analysis (SHPBA). See [19, 20] and the further comments on the application of the classic SHPBA in [6, 7] as the present paper uses the same dynamic analysis methods described in [6, 7]. The 1-wave and 2-wave analyses were used to check specimen stress-equilibrium, and the longitudinal stress was calculated by applying the 1-wave analysis. It should be noted that, since the transmission wave, ε_T, exhibited a smooth signal, the 1-wave-analysis does not require the shift and superposition of strain waves, which is an additional source of error, in contrast to the 2-wave and 3-wave analysis.

The specimen strain, ε_s, was determined in all tests by using the DIC Software GOM ARAMIS. Since homogeneous strain fields are expected to occur at the specimen centre of the unnotched specimens, the in-plane strain vector $\{\varepsilon_x,\ \varepsilon_y,\ \gamma_{xy}\}^T$ in the loading coordinate system was calculated as an average over a virtual strain gauge area [17]. The dimensions of the virtual strain gauge area were chosen to be half of the specimens' (free) length × half of the specimens width, resulting in areas of 7.5 × 5 mm^2 and 10 × 4 mm^2, for the UNC and UNT specimen configurations, respectively. In the case of DEN specimens, edge effects are expected to occur in the vicinity of the notches, which might affect the calculated strain field. Therefore, instead of using a virtual strain gauge area, the specimen strain ε_s was obtained calculating the nominal engineering strain between two facet points with an initial distance of $L/2$ along the specimen centre line. To ensure comparability, the same procedure was used to determine the specimen strain in both the quasi-static and dynamic tests. The DIC analysis parameters were chosen accordingly to the resolutions of the camera images, and are given in Tabs. 5 and 6. These parameters must be carefully chosen in a suitable balance in terms of spatial resolution and accuracy, since they have a significant influence on the displacement evaluation and strain fields reconstruction [21]. The specimen strain rate, $\dot{\varepsilon}_s[t]$, at the time t, in the loading direction, was calculated as[1]:

$$\dot{\varepsilon}_s[t] = \frac{\varepsilon_s[t] - \varepsilon_s[t-\Delta t]}{\Delta t} \tag{1}$$

in which Δt is the timestep between two data points, or consecutive DIC images.

Tensile testing of UNTS specimens ([22]) allows the calculation of the shear stress, τ_s, shear strain, γ_s, and the shear modulus, G_{xy}. Consequently, the in-plane shear strain rate, $\dot{\gamma}_s$, is calculated as:

$$\dot{\gamma}_s[t] = \frac{\gamma_s[t] - \gamma_s[t-\Delta t]}{\Delta t} \tag{2}$$

where Δt is again the timestep between two consecutive DIC images.

Table 5: ARAMIS parameters for compressive specimens.

Specimen type	Parameter	QS	HR			
			A	B	C	D
UNC	Convers. fact. [mm/pixel]	0.023	0.086	-	-	-
	Facet size [pixel^2]	17×17	10×10	-	-	-
	Facet step [pixel^2]	15×15	5×5	-	-	-
	Computation size [facets^2]	5×5	5×5	-	-	-
DENC	Convers. fact. [mm/pixel]	0.023	0.084	0.127	0.168	0.222
	Facet size [pixel^2]	17×17	10×10			
	Facet step [pixel^2]	15×15	5×5			
	Computation size [facets^2]	5×5	5×5			

[1]Throughout the text, parentheses will be used for grouping, and square brackets to surround the arguments of functions.

Table 6: ARAMIS parameters for tensile specimens.

Specimen type	Parameter	QS	HR		
			A	B	C
UNT	Conversion factor [mm/pixel]	0.019	0.105	-	-
	Facet size [pixel^2]	17×17	10×10	-	-
	Facet step [pixel^2]	15×15	5×5	-	-
	Computation size [facets^2]	5×5	5×5	-	-
UNTS	Conversion factor [mm/pixel]	0.020	0.105	-	-
	Facet size [pixel^2]	17×17	10×10	-	-
	Facet step [pixel^2]	15×15	5×5	-	-
	Computation size [facets^2]	5×5	5×5	-	-
DENT	Conversion factor [mm/pixel]	0.019	0.101	0.136	0.208
	Facet size [pixel^2]	17×17	10×10		
	Facet step [pixel^2]	15×15	5×5		
	Computation size [facets^2]	5×5	5×5		

2.3.2. Energy terms

According to Jiang and Vecchio [23], quasi-static fracture theory is applicable to dynamic cases if a condition of dynamic equilibrium is satisfied. This occurs when $E_k \ll U_{el}$ where U_{el} and E_k are the elastic and kinetic energy, respectively. These can be computed from DIC data as:

$$U_{el} = \sum_j U_{elj} = \sum_j V_j \frac{1}{2}(E_x \varepsilon_{xj}^2 + E_y \varepsilon_{yj}^2 + G_{xy}\gamma_{xyj}^2) \tag{3}$$

$$E_k = \sum_j E_{kj} = \sum_j \frac{1}{2}\rho V_j (v_{xj}^2 + v_{yj}^2) \tag{4}$$

where ε_{xj}, ε_{yj}, and γ_{xyj} are respectively the individual facet's transversal, longitudinal, and shearing strain; v_{xj} and v_{yj} are the individual facet's transversal and longitudinal velocities; V_j is the associated volume of the individual facet point; and ρ is the density of the laminate.

2.3.3. Size effect method and fracture toughness

The energy release rate associated with a crack propagating in mode I along principal direction x in a 2D orthotropic body reads [24]:

$$\mathcal{G}_I = \frac{1}{\acute{E}}\mathcal{K}_I^2 \tag{5}$$

where $\mathcal{K}_I$ is the stress intensity factor (SIF) and $\acute{E}$ is the equivalent modulus defined as:

$$\acute{E} = \left(s_{11}s_{22}\frac{1+\psi}{2}\right)^{-1/2}\lambda^{1/4} \tag{6}$$

where λ and ψ are two dimensionless elastic parameters that take into account the orthotropy of the material and that depend on the compliances, s_{ij}, as [24]:

$$\lambda = \frac{s_{11}}{s_{22}} = \frac{E_2}{E_1} \tag{7}$$

$$\psi = \frac{2s_{12}+s_{66}}{2\sqrt{s_{11}s_{22}}} = \frac{E_1E_2}{2G_{12}} - \sqrt{\nu_{12}\nu_{21}} \tag{8}$$

where E_1 and E_2 are the Young's moduli of the laminate along the two principal directions, G_{12} the shear modulus, and ν_{12} and ν_{21} are the Poisson's ratios.

If, as in the following, a balanced cross ply is used, it follows that $\lambda = 1$, and Eq. (6) reads:

$$\acute{E} = E\left(\frac{1+\psi}{2}\right)^{-1/2} \tag{9}$$

where $E = E_1 = E_2$.

For the DENT and DENC specimens, the dimensions of which are all scaled with respect to a characteristic size w, the SIF can be written as [24, 25]:

$$\mathcal{K}_I = \sigma\sqrt{w\,\kappa} \tag{10}$$

where σ is the applied remote stress, and κ is a correction factor which depends on the shape of the specimen and orthotropy of the material. Hence, for a given specimen typology (DENC or DENT), the correction factor will depend on the normalised crack length $\alpha = a/w$ (since all the other dimensions are scaled with w), and on ψ (that is the only material parameter that characterises the orthotropy, since $\lambda = 1$ for the chosen layup). If a_0 and $\alpha_0 = a_0/w$ are used to indicate the initial crack length and its normalised value, and Δa and $\Delta\alpha = \Delta a/w$ indicate the crack increment and its normalised value, it is also possible to express the correction factor as function of the crack increment, as $\kappa = \kappa\left[\alpha_0 + \frac{\Delta a}{w}, \psi\right]$.

Substituting Eq. (10) in Eq. (5) provides the expression for the energy release rate:

$$\mathcal{G}_I = \frac{1}{\acute{E}}w\sigma^2\kappa\left[\alpha_0 + \frac{\Delta a}{w}, \psi\right] \tag{11}$$

where α_0 is a constant, equal to 0.5 and 0.6 for the DENC and DENT specimens (Tab. 1), respectively.

The size-effect method requires the testing of geometrically similar specimens with *positive geometry* (i.e. specimens whose correction factor is a monotonically increasing function of α), such as DENC or DENT specimens. For these kind of specimens, unstable crack propagation occurs when the condition of tangency between the crack driving force curve, $\mathcal{G}_I$, and the resistance curve, $\mathcal{R}$, is satisfied (Fig. 5):

$$\begin{cases} \mathcal{G}_I = \mathcal{R} & (12) \\ \dfrac{\partial \mathcal{G}_I}{\partial a} = \dfrac{\partial \mathcal{R}}{\partial \Delta a} & (13) \end{cases}$$

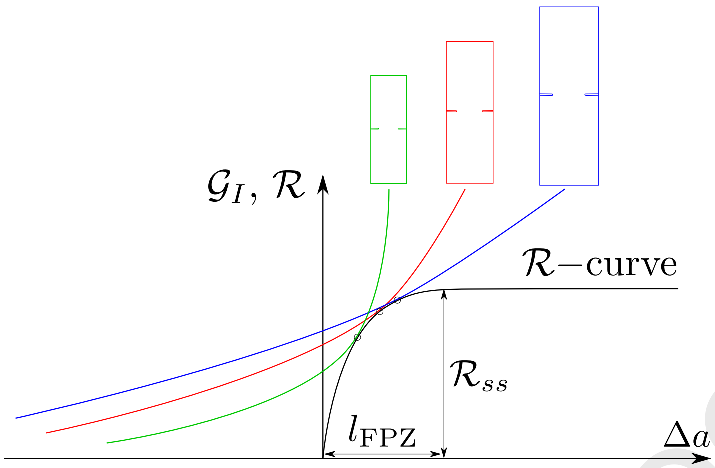

Figure 5: R-curve of the material (in black) and crack driving force curves at unstable crack propagation for specimens of different sizes.

The size-effect is a phenomenon for which the strength of the (cracked) body, σ_u, decreases with an increasing characteristic size, w. If the size effect, $\sigma_u = \sigma_u[w]$, is known, replacing σ with $\sigma_u[w]$ in Eq. (11), and the latter in Eq. (12), yields the expression of the R-curve:

$$\mathcal{R} = \frac{1}{\acute{E}} w \left(\sigma\left[w\right]\right)^2 \kappa \left[\alpha_0 + \frac{\Delta a}{w}, \psi\right] \tag{14}$$

which must hold for any w if the R-curve is considered to be a material parameter. Differentiating Eq. (14) results in:

$$\frac{\partial}{\partial w}\left(w\left(\sigma\left[w\right]\right)^2 \kappa\left[\alpha_0 + \frac{\Delta a}{w}, \psi\right]\right) = 0 \tag{15}$$

since $\partial\mathcal{R}/\partial w = 0$. Solving Eq. (15) for $w = w[\Delta a]$, and replacing this solution in Eq. 12 yields the R-curve of the laminate. This procedure allows to obtain the R-curve as the envelope of the crack driving force curves at the peak loads [26]. If the R-curve associated with the fibre fracture, $\mathcal{R}_0$, is required (i.e. for a crack propagating orthogonally to the fibre direction), by considering that the fracture toughness of the 90° plies is negligible, $\mathcal{R}_{90} \ll \mathcal{R}_0$, and keeping in mind that the laminate is a balanced cross ply (therefore half of the thickness consists of 0° plies, the other of 90° plies) a simple energetic balance yields the fracture toughness of the 0° ply as $\mathcal{R}_0 \approx 2\mathcal{R}$.

The analysis scheme employed will require the experimental determination of the elastic properties of the balanced cross ply laminate at high strain rate. Testing unnotched specimens with a layup of $[90/0]_{ns}$ will ensure the determination of the Young's modulus of the laminate (in both tension, E_t, and compression, E_c). Additionally, the tensile test of the $[\pm 45]_{2s}$ will allow the determination of the shear modulus of the laminate, G_{12} (that for the particular layup used is also the shear modulus of the ply). It should also be observed that since in tension and compression the material will exhibit different values of the Young's modulus, the dimensionless parameter ψ will assume different values in tension and compression, ψ_t and ψ_c, respectively. Thus, the correction factor κ, will also differ for tension and compression (κ_t and κ_c, respectively), because of the asymmetry of the material in tension and compression (i.e. different values of ψ), and also because of the different geometry of the specimens. The calculation of κ is done numerically and is not reported here for the sake of conciseness (full details are found in [6, 7, 9, 10]).

Finally, it should be noted that this methodology relies on the accurate determination of the size effect that consists of testing geometrically similar specimens and finding the relation between the strength and the characteristic size, using appropriate fitting functions [10, 26] (Tab. 7).

Table 7: Size effect law fits [26].

Regression fit	Formula	Fitting parameters	R_{ss}	l_{fpz}
Linear regression I	$\frac{1}{\sigma_u^2} = mw + q$	m, q	$\frac{\kappa_0}{\acute{E}}\frac{1}{m}$	$\frac{f_0}{2\acute{f}_0}\frac{q}{m}$
Linear regression II	$\frac{1}{w\sigma_u^2} = \acute{m}\frac{1}{w} + \acute{q}$	$\acute{m}$, $\acute{q}$	$\frac{\kappa_0}{\acute{E}}\frac{1}{\acute{q}}$	$\frac{f_0}{2\acute{f}_0}\frac{\acute{m}}{\acute{q}}$
Bilogarithmic	$\ln\sigma_u = \ln\frac{M}{\sqrt{N+w}}$	M, N	$\frac{\kappa_0}{\acute{E}}M^2$	$\frac{f_0}{2\acute{f}_0}N$

3. Experiments and discussion

3.1. Unnotched specimens: determination of the in-plane material properties

3.1.1. Longitudinal compression

The stress-strain curves for the UNC specimens for QS and HR loading are presented in Fig. 6(a) and Fig. 6(b), respectively. An approximately linear stress-strain behaviour with low scatter is observed at both investigated strain rate regimes. The strain rate of the dynamic tests, calculated using Eq. 1 on basis of the strain data from DIC, is in the desired order of about 100 s^{-1} (indicated with the label `UNC_HR_x_SR` in Fig. 6(b)). A slight decrease of the strain rate over time is observed and is also indicated by the falling tendency of the reflected-wave signal in Fig. 7(a) in the range between about 5.5×10^{-4} and 7.3×10^{-4} s. The 1-wave and 2-wave stress curves of a representative HR test are plotted in Fig. 7(b), showing that the UNC specimens characterized using the SHPB are under stress equilibrium conditions.

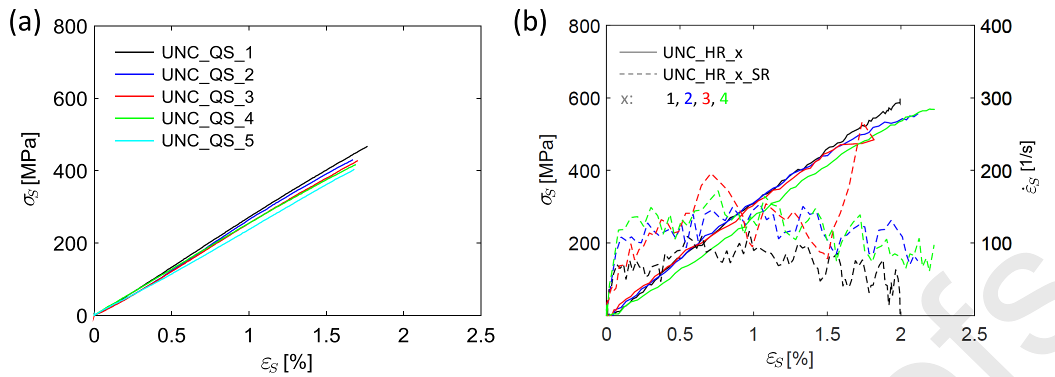

Figure 6: Compressive stress-strain curves in the longitudinal direction for QS (a) and HR (b) loading.

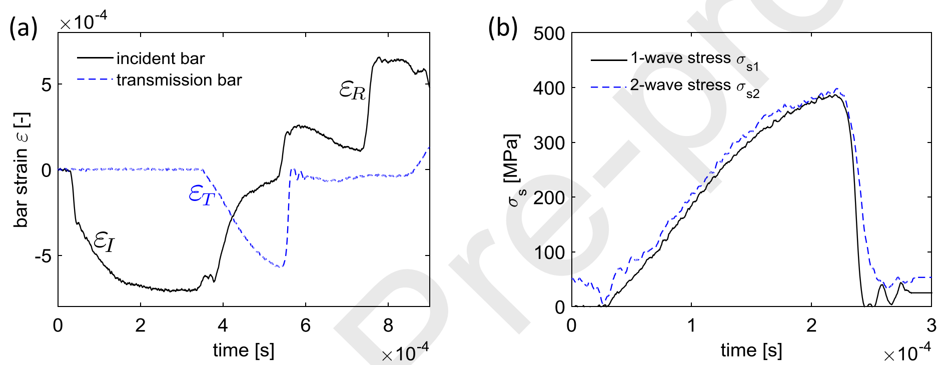

Figure 7: Bar strain wave group of an SHPB UNC test (a) and dynamic stress equilibrium check (b).

Both the QS and the HR specimens show a homogeneous strain distribution until the point of sudden failure (Fig. 8). Two of the five UNC specimens under QS loading conditions failed within the free length (Fig. 8(d)). The remaining QS and all the HR tested UNC specimens showed invalid end face splitting failure (Fig. 8(h)). However, this does not affect the reliable determination of the compressive Young's modulus of the cross-ply laminate E_c, and is therefore not critical in the context of the presented work. The simple UNC specimen geometry, obtained from the same laminate as used for the DENC tests, was ideal for the determination of the quasi-static and dynamic compressive Young's modulus. A more suitable specimen geometry and methodology to measure the strain rate effect on the longitudinal compressive strength of fibre-reinforced polymers is presented in [27]. As already done in [6], the gradient of the stress-strain curves was analysed in a region where the strain rate has reached an approximately constant level and well in advance of the point of specimen failure. Considering the strain rate curves of Fig. 6(b), the compressive stiffness of the laminate under HR loading was calculated between ε_s=0.4% and 0.9% and, for consistency, the same region was used for the calculation of E_c from the QS test.

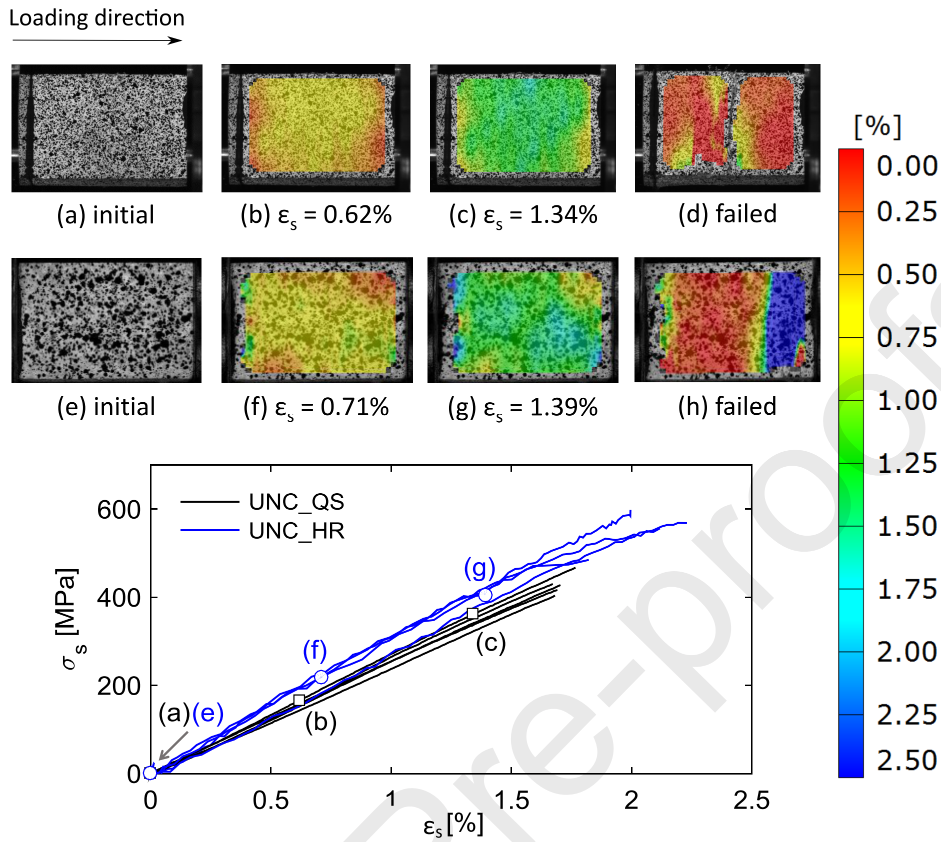

Figure 8: Stress strain curves in compression and longitudinal strain fields for a representative specimen in QS (a)-(d) and HR (e)-(h) loading.

The calculated values of E_c under QS and HR loading are listed in Tabs. 8 and 9, respectively. As shown in Fig. 8, where the stress-strain curves of all UNC tests are displayed together, the compressive Young's modulus of the cross-ply laminate under dynamic loading is higher than that observed for the QS reference case. As shown in Fig. 9, this is consistent with the results in literature, even though the observed strain rate effect (15% increase at $\dot{\varepsilon}_s = 125$ s^{-1}) is less pronounced than that reported by Shokrieh and Omidi [28] for a glass/epoxy material. Regarding the strain rate sensitivity of E_c, it can be concluded that the GFRP material system under consideration in this study shows significantly different behaviour than that of the CFRP material system investigated in [17], where no effective strain rate effect was found for E_c. The measured ultimate stress values σ_u are also listed in Tabs. 8 and 9 but should be treated with care. Despite the presence of a predominantly premature failure mode, an increasing σ_u was observed with increasing strain rate; this is consistent with the results from other studies [28–30].

Table 8: Summary of the experimental results of the QS UNC tests.

Specimen ID	E_c [MPa]	σ_u [MPa]	failure mode
UNC_QS_1	27814	466.4	compressive FF (free length)
UNC_QS_2	28097	429.4	compressive FF (free length)
UNC_QS_3	26817	426.9	layer splitting (end face)
UNC_QS_4	25250	415.8	layer splitting (end face)
UNC_QS_5	24330	403.0	layer splitting (end face)
mean	26462	428.3	
STDV	1631.0	23.7	
CV [%]	6.2	5.5	

Table 9: Summary of the experimental results of the HR UNC tests.

Specimen ID	E_c [MPa]	σ_u [MPa]	failure mode
UNC_HR_1	31389	599.5	layer splitting (end face)
UNC_HR_2	32289	556.8	layer splitting (end face)
UNC_HR_3	28480	485.3	layer splitting (end face)
UNC_HR_4	29324	573.1	layer splitting (end face)
mean	30371	553.6	
STDV	1768.9	48.9	
CV [%]	5.8	8.8	

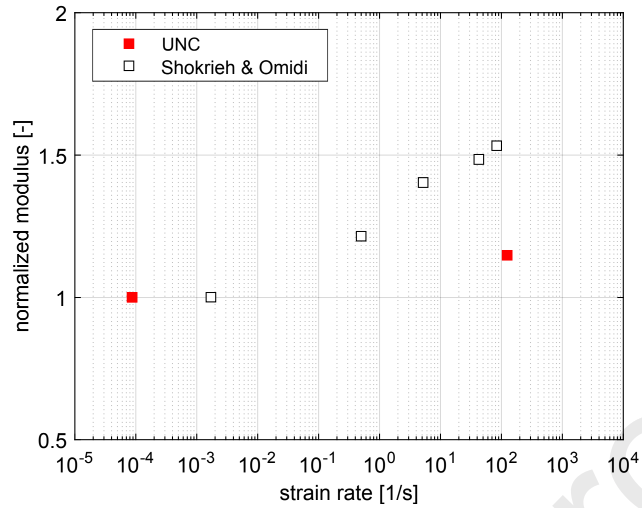

Figure 9: Normalized compression Young's modulus; obtained results and comparison with literature.

3.1.2. Longitudinal tension

The stress-strain curves of the QS UNT specimens (Fig. 10(a)), show a slightly bilinear behaviour, with a change in slope occurring at about $\varepsilon \approx 0.6\%$. This might also be present under dynamic loading conditions (Fig. 10(b)), but it cannot be affirmed with certainty since the original strain signal shows some oscillations until $\varepsilon \approx 0.8\%$. This change in modulus appears to be characteristic for tensile loaded glass-epoxy materials in fibre direction, as it was also found for both glass-epoxy UD [31] and weave [32] materials under QS and HR loading. The stress-strain curves of both the QS and the HR tests are plotted until the point of maximum stress; however, while the QS specimens showed fibre failure (FF), the HR specimens failed at the adhesive bond, within the adapter and the last plotted data points in Fig. 10(b) do not represent the tensile strength of the laminate under HR loading.

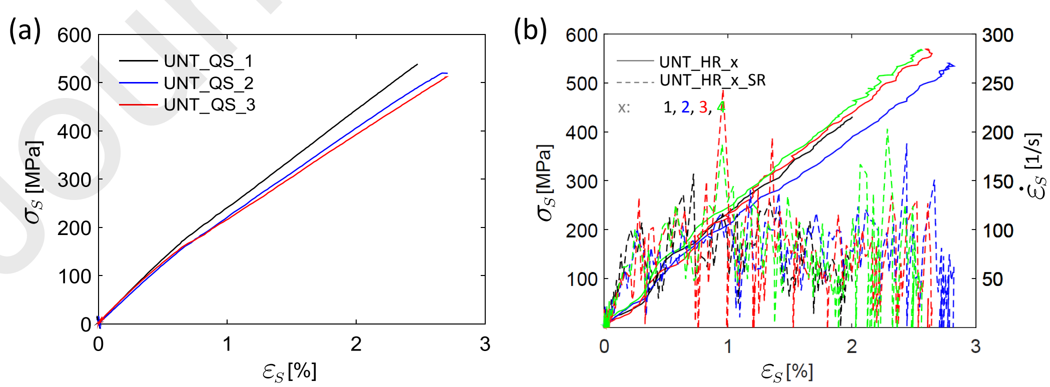

Figure 10: Tensile stress-strain curves in the longitudinal direction at QS (a) and HR (b) loading.

The strain rate curves, plotted in Fig. 10(b) indicate that, despite the presence of some noise, all the HR specimens were tested at the same strain rate, $\dot{\varepsilon}_s \approx 80\ \mathrm{s}^{-1}$. The suitability of the chosen set-up parameters can be further seen in Fig. 11(b), where the stress equilibrium condition is shown to be fulfilled for the HR UNT tests. In addition, the curves in Fig. 11 demonstrate the practicability and the benefit of using the overlapping correction introduced in [7].

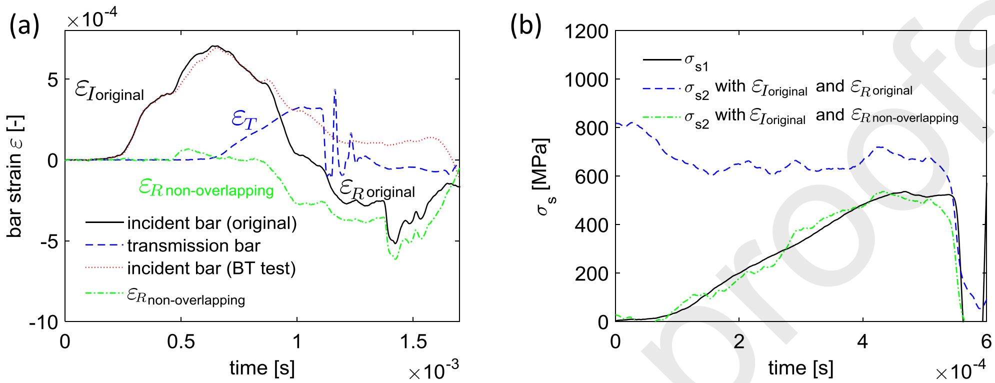

Figure 11: Bar strain wave group of SHTB UNT test (a) and dynamic stress equilibrium check (b).

Plotting the stress-strain curves for both QS and HR loading in one diagram (Fig. 12) shows there is no significant strain rate sensitivity for the tensile Young's modulus. It should be noted that the analysis scheme employed assumes the material to be linear elastic. Therefore, although the tensile Young's modulus (calculated in the first linear region of the stress-strain curve) is equal to 32820 MPa, in the following, a value of $E_t = 21500$ MPa is used. This is calculated performing a linear fit of the experimental data (Fig. 12).

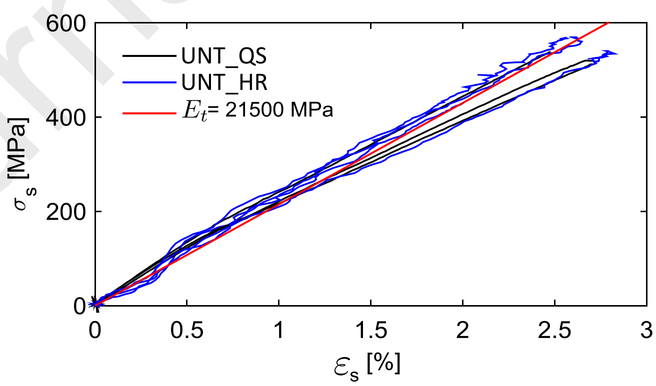

Figure 12: Tensile stress-strain curves in the longitudinal direction at QS and HR loading, and curve with average Young's modulus.

This result is in good agreement with what was reported by Adams and Adams [33], and Shokrieh

215 and Omidi [34], who reported a very slight decrease and increase of E_t with increasing strain rate, respectively (Fig. 13). In contrast, Gerlach et al. [35] found a very pronounced strain rate sensitivity of the tensile Young's modulus for GFRP (Fig. 13).

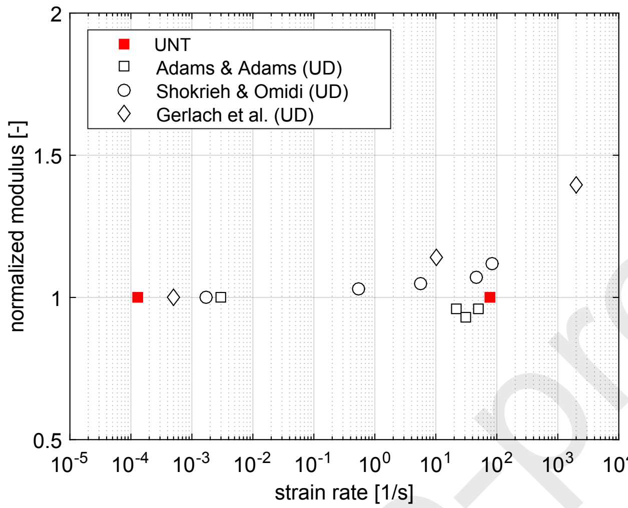

Figure 13: Normalized tensile Young's modulus and comparison with literature data.

The tensile strengths of the QS UNT specimens are presented in Tab. 10. No strength values of the HR tests related to the desired tensile FF mode can be reported due to the failure of the adhesive
220 bonding within the adapters. However, despite the premature failure of the HR UNT specimens, all the specimens which were tested using the SHTB exceeded the strength level found from the QS tests, and therefore, it can be concluded that the tensile strength is strain rate sensitive. Corresponding results can be found in literature, describing a slight [33] or pronounced [30, 31, 34] increase of the longitudinal tensile strength of GFRPs with increasing strain rate.

Table 10: Summary of the experimental results of the QS GFRP UNT CP0 tests.

Specimen ID	σ_u [MPa]	failure mode
UNT_QS_1	537.8	tensile FF (free length)
UNT_QS_2	519.8	tensile FF (free length)
UNT_QS_3	511.8	tensile FF (free length)
mean	523.1	
STDV	13.3	
CV [%]	2.5	

3.1.3. In-plane shear

The QS and HR shear stress-strain curves exhibit a characteristic non-linear behaviour as expected (Fig. 14). While the QS curves are plotted until the point of ultimate failure, the HR curves are presented until the point of maximum stress, as the loading pulse of the SHTB setup was insufficiently long to cause the failure of the UNTS specimens. Taking a closer look at the bar strain waves (Fig. 15(a)), it can be observed that the initial gradient of the incident-wave, ε_I, is larger than that of the transmitted-wave, ε_T, and this corresponds to an ascending trend in the strain rate (Fig. 14(b)). Even if a flattening of the incident-wave could not be obtained with the available pulse shapers, the shear strain rate was found to be in an acceptable range from 100 to 400 s^{-1}. The dynamic stress equilibrium check ((Fig. 15(b)) shows satisfactory consistence of the 1-wave and 2-wave stresses, and the difference at the rear part of the curves is caused by the decreasing loading pulse, and lies in a section that is not considered in the analysis of the HR tests.

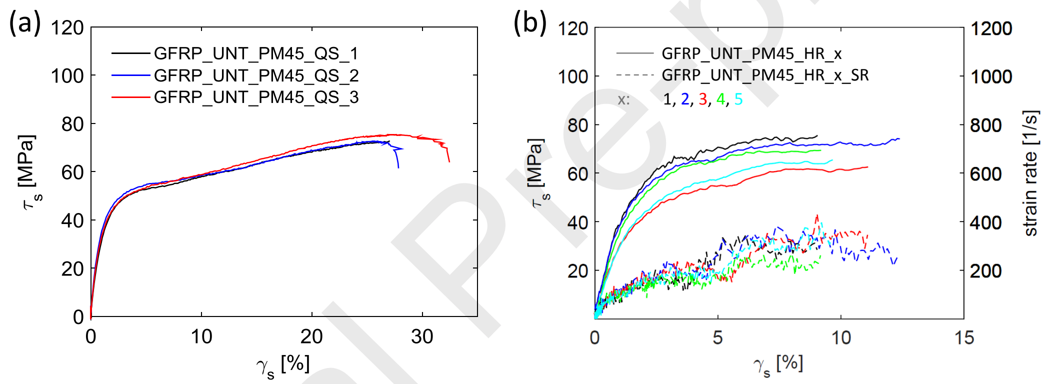

Figure 14: Shear stress-shear strain curves at QS (a) and HR (b) loading.

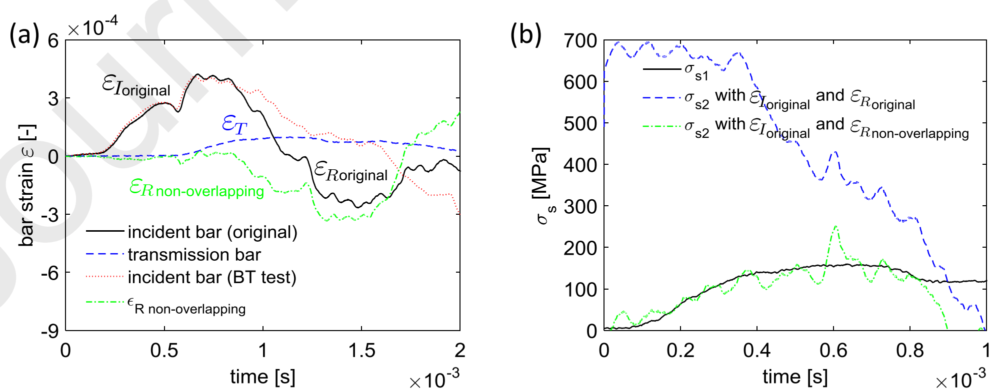

Figure 15: Bar strain wave group of an STPB UNTS test (a) and dynamic stress equilibrium check (b).

According to DIN EN 14129 [22], the shear stress-shear strain curves are analysed only in the region where $\gamma \leq 5\%$. Fig.16 shows the appropriate section for the measured QS and HR curves, all combined in a single diagram. For all the QS UNTS specimens, a consistent shear damage failure mode was observed. As previously mentioned, the HR specimens could not be loaded until ultimate fracture at the SHTB; nevertheless some damage was clearly visible.

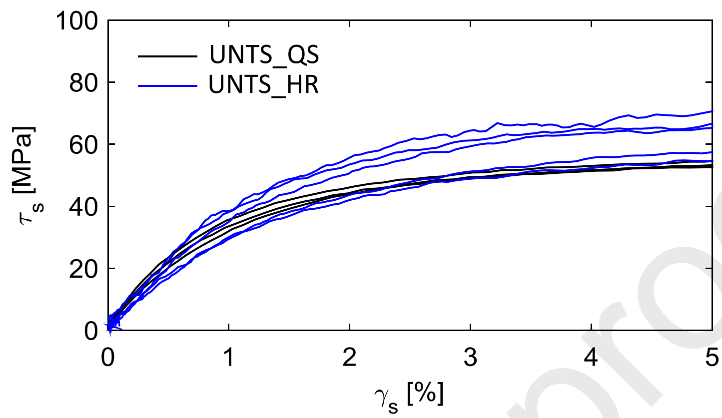

Figure 16: Shear stress-shear strain curves at QS and HR loading for $\gamma \leq 5\%$.

As recommended in DIN EN 14129 [22], the in-plane shear modulus, G_{12}, should be calculated in the initial linear part of the shear stress-shear strain curve. For the data reduction of the QS specimens, G_{12} was calculated in the section between $\gamma_s = 0.2 - 0.5\%$. The same range was not used for the determination of the in-plane shear modulus under dynamic loading, as the specimen is highly accelerated in the early phase of the test, as indicated by the sharp increase of the strain rate-time curve. G_{12} of the HR tests was therefore calculated as the slope of the secant between γ_s=0.4% and 0.7%, where $\dot{\gamma_s}$ in the order of $\dot{\gamma_s} \approx 80$ s^{-1}, with a slightly rising trend, and the shear stress-shear strain curve is still approximately linear. Tabs. 11 and 12 list the calculated in-plane shear modulus G_{12} for the QS and HR cases, respectively. In addition, the related in-plane shear strength, S_{12}, calculated in accordance to DIN EN 14129 [22] is given.

Table 11: Summary of the experimental results of the QS UNTS tests.

Specimen ID	G_{12} [MPa]	S_{12} [MPa]	failure mode
UNTS_QS_1	3351	52.6	IFF (free length)
UNTS_QS_2	3950	54.4	IFF (free length)
UNTS_QS_3	3639	53.2	IFF (free length)
mean	3646	53.4	
STDV	299.6	0.9	
CV [%]	8.2	1.7	

Table 12: Summary of the experimental results of the HR UNTS tests.

Specimen ID	G_{12} [MPa]	S_{12} [MPa]	failure mode
UNTS_HR_1	4293	70.6	no ultimate failure
UNTS_HR_2	4245	66.5	no ultimate failure
UNTS_HR_3	2508	54.8	no ultimate failure
UNTS_HR_4	3577	65.2	no ultimate failure
UNTS_HR_5	2948	57.4	no ultimate failure
mean	3514	62.9	
STDV	832.4	6.6	
CV [%]	23.7	10.5	

The results show an insignificant strain rate effect on the in-plane shear modulus (4% decrease), and a substantial effect on the in-plane shear strength (18% increase). It should be noted that, while the HR G_{12} values were obtained at $\dot{\gamma_s} \approx 80$ s^{-1}, the HR S_{12} values can be assigned to a shear strain rate in the order of ≈ 220 s^{-1}. Marginal decreases of G_{12} with increasing shear strain rates was also found by Shokrieh and Omidi [36], while Gerlach et al. [35] reported a strain rate insensitivity for G_{12} (Fig. 17(a)). For what concerns the strain rate sensitivity of S_{12}, this also agrees with other studies [35–37] which have however reported a more pronounced strain rate sensitivity (Fig. 17(b)).

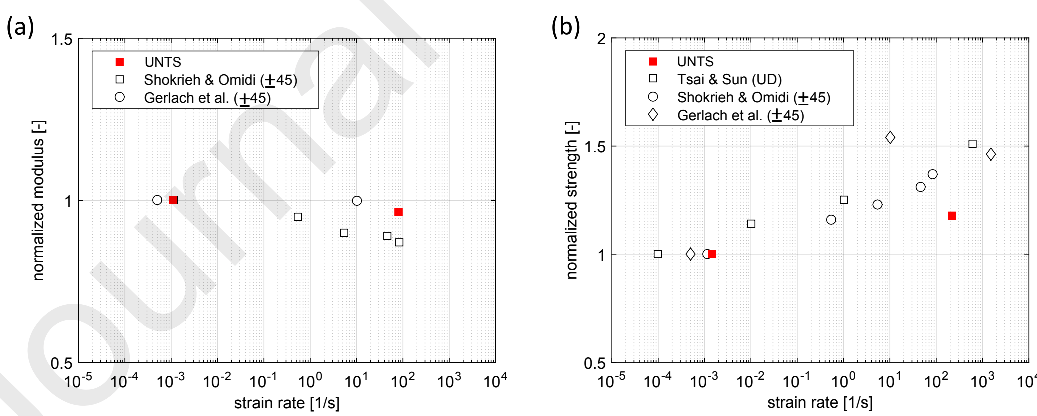

Figure 17: Normalized (a) in-plane shear modulus and (b) in-plane shear strength as a function of the strain rate, and comparisons with literature.

3.1.4. Summary of elastic properties

The elastic properties of the GFRP cross ply laminate, used for the calculations of the fracture toughness parameters, are shown in Tab. 13.

Table 13: Elastic properties of the GFRP cross ply laminate.

Strain rate regime	E_c [GPa]	E_t [GPa]	G_{12} [GPa]	ν_{12} [-]	ψ_c [-]	ψ_t [-]
QS	26.5	21.5	3.6	0.14	2.81	3.49
HR	30.4	21.5	3.5	0.15	2.92	4.17

3.2. Notched specimens: determination of the fracture properties

3.2.1. Double edge notched compression (DENC)

The transparency of the GFRP laminate was used to assess the extent of the damaged regions
265 before unstable crack propagation. Fig. 18 shows the images of a specimen of size D during compression loading in the electro mechanical testing machine, without a sprayed speckle pattern on the specimen's surface.

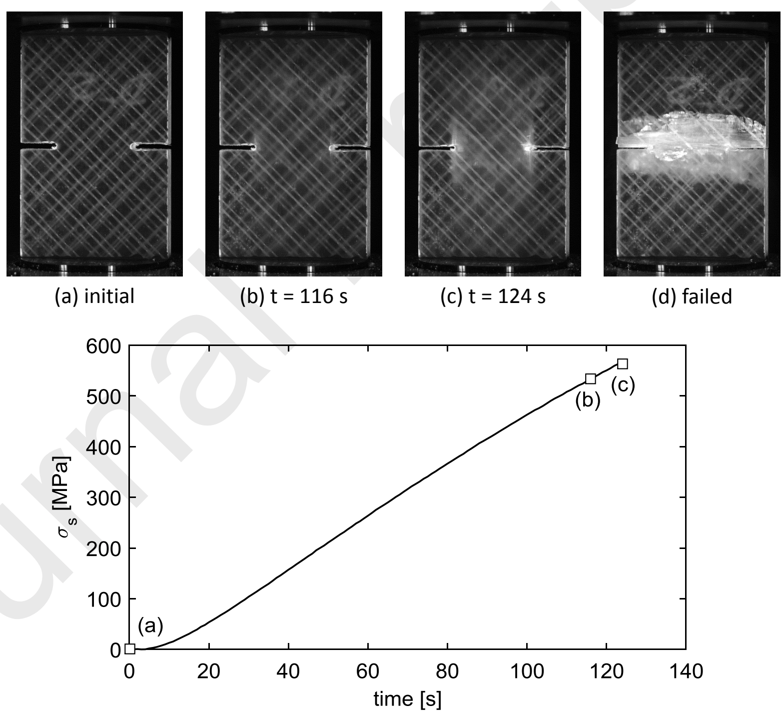

Figure 18: DENC specimen during QS compression loading and corresponding stress-time curve.

The images and the corresponding stress-time curve indicate that no overall damage (indicated by the clouded regions in Fig. 18) occurs prior to unstable fracture, thus validating the use of the size-effect
270 method for the evaluation of the intralaminar fracture toughness. After failure, the specimens exhibit a crushed zone in the ligament of the specimen, as expected (Fig. 18(d)). Some delamination is also

present in the failed specimen, but this only occurs after unstable crack propagation, and therefore it does not affect the correct calculation of the intralaminar fracture toughness.

Similar failure mechanisms are also found for the HR specimens for which a post-mortem analysis revealed a larger crushed region in the the centre of the specimen. However, this is due to the fact that a SHPB is used, and therefore, the specimen will be loaded several times after the actual test has finished. This was clarified by using a high speed camera (Photron FASTCAM SA-Z) throughout the test (Fig.19). When the unstable crack propagation is reached (Fig.19(b)), the failure is localised within the ligament, and propagates to the other regions of the specimens starting during the passing of the second wave (Fig.19(c)). Even if a detailed comparison of the fracture surfaces for the QS and HR specimens is not possible, experimental evidence indicates that the failure mechanism at QS and HR is similar, and substantial damage only occurs after peak load. This statement is also supported by the fact that the axial stress-strain curves, at both QS and HR loading, show a nearly linear behaviour until peak load (Fig. 20(a)), and similarly stable strain fields (Fig. 20(b)).

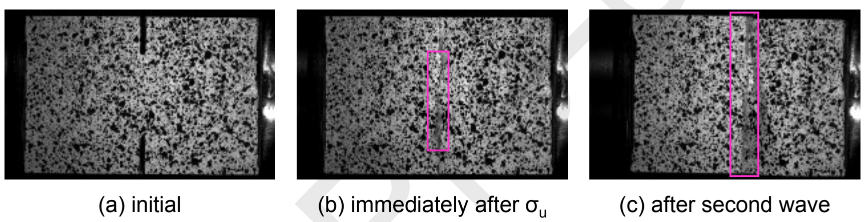

Figure 19: DENC specimens during HR compression loading.

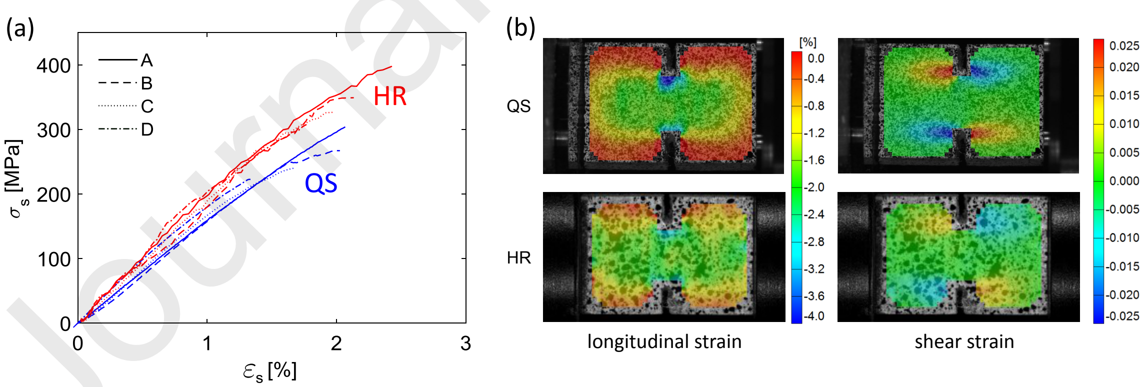

Figure 20: Stress-strain response for QS and HR loading of DENC specimens.

Figs. 21(a,c) present the bar strain waves of the SHPB tests for the DENC specimen sizes A and D, respectively. The comparison of the incident-bar signals obtained from the original test (black curve) and from the bars-together (BT) test (red curve) show that the incident-wave is not completely subsided when the reflected wave also arrives at the strain gauge terminal. The strain gauge terminal is positioned halfway along the incident-bar. The long duration of the incident-wave is caused by the use of a long striker-bar (0.8 m) in combination with pronounced pulse shaping. As a result, the measured reflected- wave during a HR test is superposed by a remaining compressive strain amount of the incident wave (and vice-versa), making a reliable stress equilibrium check, according to the classic split-Hopkinson pressure bar analysis (SHPBA), unfeasible (Figs. 21(b,d)). The superposition correction method (see [6] for more details) is used in order to reconstruct the non-overlapping shape of the reflected-wave. Calculating the 2-wave stress σ_{s2} based on $\varepsilon_{R\ \text{non-overlapping}}$ leads to very good correlation of the calculated stress-time curves at both specimen/bar interfaces ((Figs. 21(b,d)). One reason for the good correlation can be seen in the excellent reproducibility of the incident-wave when using copper pulse shapers, allowing a very reliable reconstruction of $\varepsilon_{R\ \text{non-overlapping}}$ (Figs. 21(a,c)).

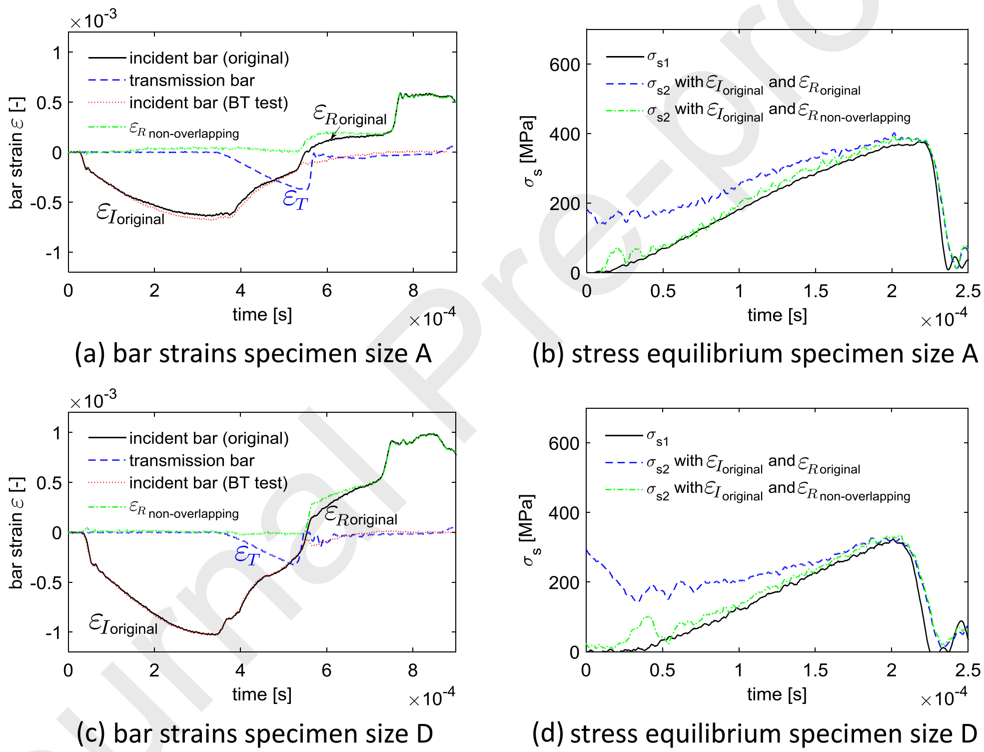

Figure 21: Bar strain wave group of a SHPB DENC test, and dynamic stress equilibrium check for specimens of sizes A (a,b) and D (c,d).

Under both QS and HR loading, the ultimate stress σ_u decreases with increasing characteristic size w (Tab. 14). The HR strength of the DENC specimens of size A, B, C and D, is found to be 35%, 41%, 39% and 42% higher than under QS loading, respectively. This is a more pronounced strain rate effect than that observed for the IM7-8552 material (average increase of 28.8%) at a comparable strain rate [6]. The strain rate curves of the DENC specimens shows that a constant strain rate is quickly achieved during the test (Fig. 22), hence ensuring a reliable derivation of the size effect law.

Table 14: Summary of the experimental results of the DENC tests.

		A	B	C	D
	w [mm]	5	7.5	10	12.5
QS	σ_u [MPa]	284.9	247.8	231.1	222.7
	STDV (σ_u) [MPa]	17.5	14.4	12.4	7.2
	CV (σ_u) [%]	6.1	5.8	5.4	3.2
HR	σ_u [MPa]	383.8	350.2	321.9	316.8
	STDV (σ_u) [MPa]	8.2	10.7	6.0	14.4
	CV (σ_u) [%]	2.1	3.1	1.9	4.5

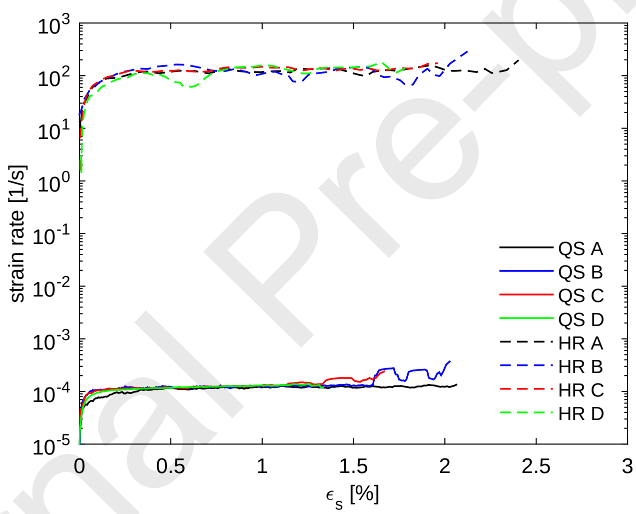

Figure 22: Specimen strain rate curves for QS and HR loading.

305 Fracture occurred when the specimens were in dynamic equilibrium (i.e. when $E_k \ll U_{el}$), as shown in Fig. 23 for QS and HR loading. While the kinetic energy is nearly constant for the QS case, for the HR loading the kinetic energy E_k increases, due to the rigid body movement. However, this does not affect the calculation of the fracture parameters.

The experimental data from the DENC tests (Tab. 14) and the corresponding best fitting curves for the recommended linear I, linear II and bilogarithmic fitting functions (Tab. 7) are presented in Tab. 15. Judging by the coefficient of determination (R^2) all the considered fitting functions provided an excellent fitting (Fig. 24(a)).

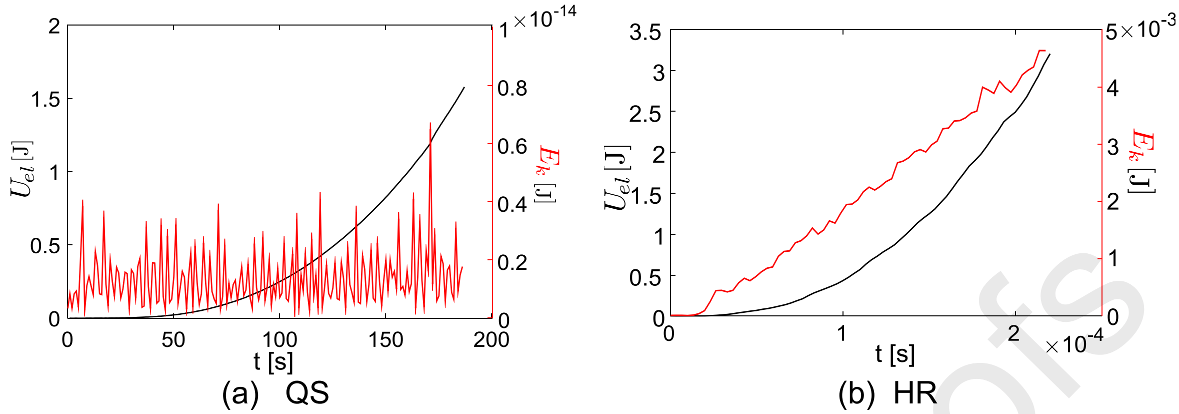

Figure 23: Strain and kinetic energy terms for (a) QS and (HR) loadings (specimen size A).

Table 15: Regression fitting parameters for the size effect law of the GFRP DENC specimens.

Regression fit	Parameter	QS	HR
Linear regression I	m [MPa^{-2}mm^{-1}]	1.04× 10^{-6}	4.41 × 10^{-7}
	q [MPa^{-2}]	7.78× 10^{-6}	4.78× 10^{-6}
	R^2 [-]	0.954	0.944
Linear regression II	$\acute{m}$ [MPa^{-2}]	6.80× 10^{-6}	4.44× 10^{-6}
	$\acute{q}$ [MPa^{-2}mm^{-1}]	1.16× 10^{-6}	4.82× 10^{-7}
	R^2 [-]	0.942	0.980
Bilogarithmic	M [MPa$\sqrt{\text{mm}}$]	951	1474
	N [mm]	6.52	10.01
	R^2 [-]	0.958	0.956

The pronounced strain rate effect on the nominal strength σ_u (Fig. 24(a)), is reflected by a substantial increase in fracture toughness (Fig. 24(b)). The steady-state value of the R-curve for the ply R_0^{ss} (Tab. 16), is 2.2 times higher in the HR case with respect to the QS reference case. The length of fracture process zone, l_{fpz}, (Tab. 16), also increases under dynamic conditions by about 51%.

Following [26], it is convenient to fit the R-curve with the following analytical expression:

$$\begin{cases} R_0 = R_0^{ss}\left[1-(1-\beta\Delta a)^n\right] & if\Delta a < l_{fpz} \\ R_0 = R_0^{ss} & if\Delta a \geq l_{fpz} \end{cases} \tag{16}$$

where β and n are two material parameters (Tab. 17). Since the values of β, n, and R_0^{ss}, are virtually the same, it is concluded that the R-curve will not substantially depend on the fitting function used for the size effect law.

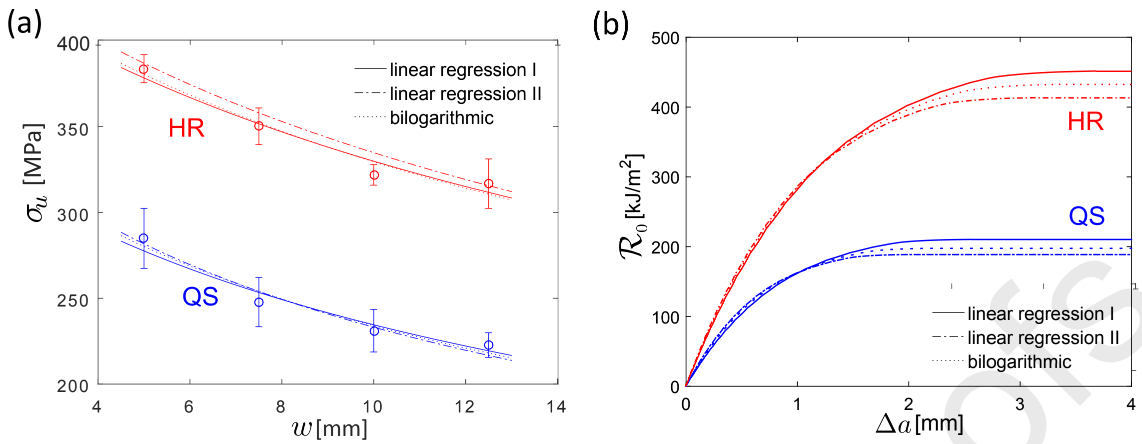

Figure 24: (a) Size effect law and (b) R-curves for QS and HR loading in compression.

Table 16: Summary of the fracture toughness properties for longitudinal compressive failure.

Regression fit	Property	QS	HR
Linear regression I	R_0^{ss} [kJ/m^2]	210.3	451.3
	l_{fpz} [mm]	2.57	3.69
Linear regression II	R_0^{ss} [kJ/m^2]	188.7	413.2
	l_{fpz} [mm]	2.01	3.14
Bilogarithmic	R_0^{ss} [kJ/m^2]	197.6	432.4
	l_{fpz} [mm]	2.23	3.40

Table 17: Coefficient for the analytical expression of the R-curve in compression.

Regression fit	Fitting parameter	QS	HR
Linear regression I	β [mm^{-1}]	0.3038	0.2115
	n [-]	4.108	4.133
Linear regression II	β [mm^{-1}]	0.3876	0.2486
	n [-]	4.110	4.133
Bilogarithmic	β [mm^{-1}]	0.3492	0.2290
	n [-]	4.108	1.133

3.2.2. Double edge notched tension (DENT)

Representative images of fractured DENT specimens, tested at QS and HR strain rates, are shown in Fig. 25. At least three valid tests were conducted for each specimen size and at each strain rate regime. Very similar macroscopic failure modes were obtained regardless of the specimen size and loading velocity. Fracture of the specimens was observed in the ligament of the specimens, and was characterised by fibre fracture and fibre pull-out at both strain rates. The comparison of Fig. 25(a) with 25(b) indicates that fibre-pull out is slightly more pronounced in the dynamically tested specimens. However, the failure pattern of the HR specimens might be distorted, as the already broken specimen halves were subsequently pressed together due to compression strain waves, which were travelling within the SHTB after the actual tension tests were already finished. This undesired reloading of the specimen is further supposed to be the reason for the delaminations that are observed over the entire specimen width for HR specimens of all three sizes (Fig. 25(b)).

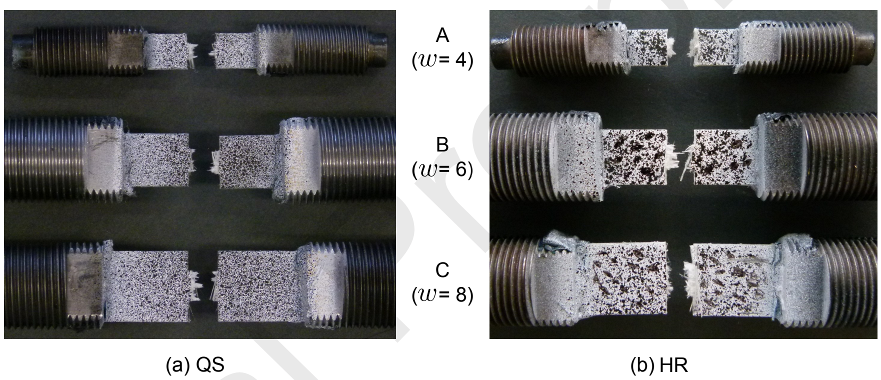

Figure 25: Failed GFRP DENT specimens after QS and HR loadings.

The stress-strain curves at both investigated strain rates (Fig. 26(a)) exhibit a slightly bi-linear behaviour for small deformations, as similarly observed for the UNT specimens (Fig. 12), and substantial non linearity at large strains (in proximity of the peak load). This can be explained from the damage mechanisms (fibre fracture and fibre pull-out) that are associated with the stable crack propagation (before unstable crack propagation occurs at peak load). The strain rate curves (Fig. 26(b)) show a slight increase over time, which might be attributed to the fact that the gradient of the incident-pulse can not be flattened to the necessary extent by using the available pulse shaping options. This is clearly visible when comparing the gradient of the incident- and transmitted-bar waves (Fig. 27), which should be equal in order to reach a constant strain rate in the specimen. It should be observed that, for both QS and HR loading rates, the respective strain rates are virtually independent of the size of the tested specimens.

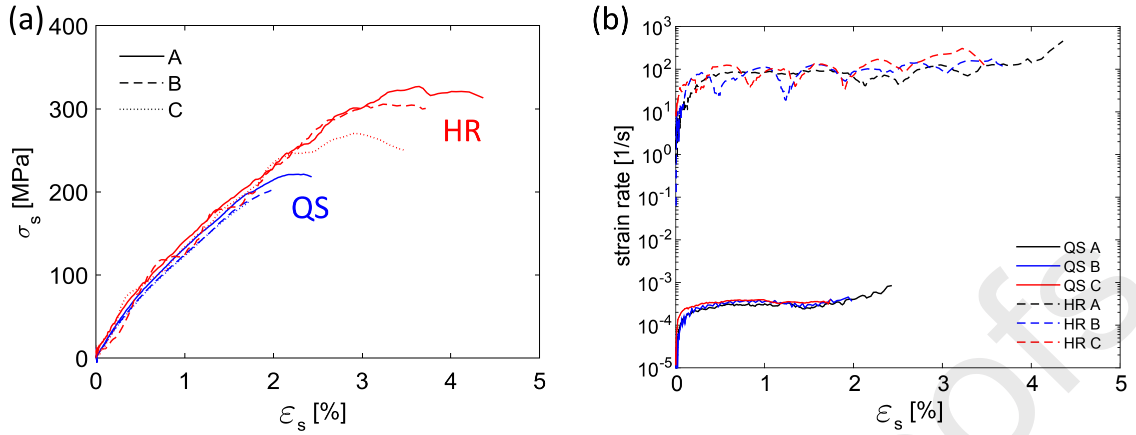

Figure 26: Stress-strain and strain rate-strain curves for DENT specimen under QS (a) and HR (b) loading.

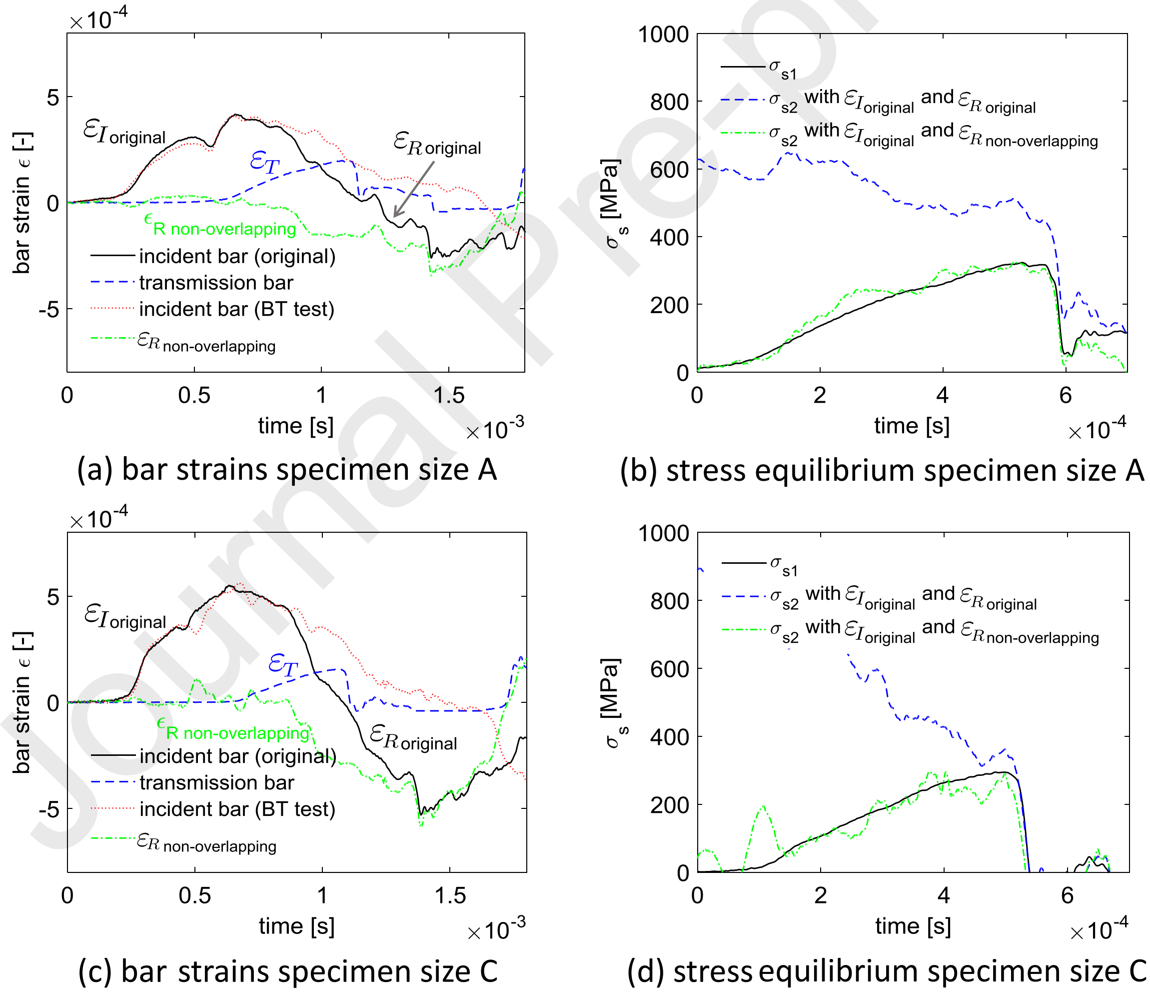

Figure 27: Bar strain wave group of an SHTB DENT test and dynamic stress equilibrium check for representative GFRP DENT specimens of size A (a,b) and C (c,d).

Figs. 27(a,c) show the bar strain wave groups of an SHTB test for representative DENT specimens of size A and C, respectively. When comparing the measured incident-bar curves from the actual tests (in black) with the incident-bar curves from the corresponding BT-tests (in red), it can be noted that an accurate reproducibility of the incident-pulse is not possible when using extreme pulse shaping in combination with very high striker velocities. While this is not critical for the validity of each individual SHTB test, using the wave superposition correction method is only possible to a limited extent. However, even in this case, a rough evaluation of the stress-equilibrium can be made, while the classical SHPBA equilibrium check fails (Fig. 27(b,d)). A very good correlation of σ_{s1} and σ_{s2} can be found for specimen size A when using the superposition correction method (Fig. 27(b)). This is not surprising taking into account that a lower striker-bar velocity was used for specimen size A than for specimen sizes B and C (Tab. 4), resulting in more reproducible incident-wave signals (Fig. 27(a)).

A size effect is observed for the nominal strength, σ_u, for both QS and HR loading (Tab. 18). The test results also show a pronounced strain rate effect for σ_u, which is on average equal to 43%, 44% and 52% for specimens of size A, B and C, respectively.

Table 18: Summary of the experimental results for the DENT tests.

		A	B	C
	w [mm]	4	6	8
QS	σ_u [MPa]	218.2	207.7	189.6
	STDV (σ_u) [MPa]	10.6	9.7	8.1
	CV (σ_u) [%]	4.9	4.7	4.3
HR	σ_u [MPa]	312.1	299.2	287.5
	STDV (σ_u) [MPa]	11.0	4.4	11.6
	CV (σ_u) [%]	3.5	1.5	4.0

The strain and kinetic energy curves for a DENT specimen of size C for both QS and HR loadings are presented in Fig. 28. It is observed that the dynamic equilibrium has been reached since the overall strain energy, U_{el}, under HR loading, was found to be significantly higher than the kinetic energy, E_k. Again, it is observed that the kinetic energy, E_k, increases during the HR test, and this is due to the rigid body movement of the specimen.

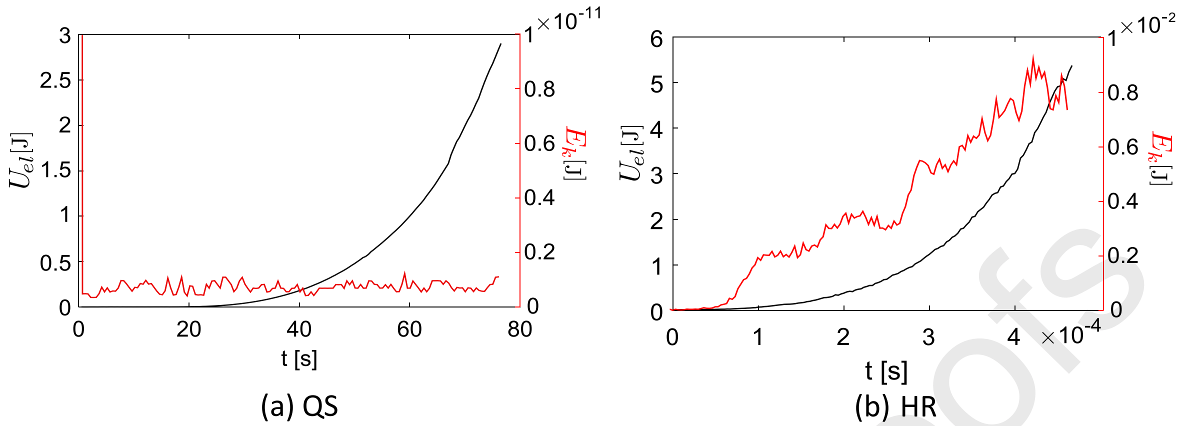

Figure 28: Strain and kinetic energy terms for (a) QS and (HR) loadings (specimen size C).

For the determination of the size effect law, the experimental data (Tab. 18) was fitted using the linear regression I, linear regression II, and bilogarithmic laws (Tab. 28 and Fig. 29(a)).

Table 19: Regression fitting parameters for the size effect law in tension.

Regression fit	Parameter	QS	HR
Linear regression I	m [$MPa^{-2}mm^{-1}$]	1.70×10^{-6}	4.58×10^{-7}
	q [MPa^{-2}]	1.38×10^{-5}	8.43×10^{-6}
	R^2 [-]	0.958	1.000
Linear regression II	$\acute{m}$ [MPa^{-2}]	1.45×10^{-7}	8.44×10^{-6}
	$\acute{q}$ [$MPa^{-2}mm^{-1}$]	1.57×10^{-6}	4.57×10^{-7}
	R^2 [-]	0.984	1.000
Bilogarithmic	M [$MPa\sqrt{mm}$]	779	1479
	N [mm]	8.57	18.44
	R^2 [-]	0.956	1.000

The determination of the size effect law allows the calculation of the R-curve associated with the
365 longitudinal failure in tension (Fig. 29(b)). A very pronounced strain rate effect can be observed, as expected, indicating that, contrarily to what happens for carbon fibre, the glass fibre is strain rate sensitive in tension.

Again it should be observed how the determined fracture properties are virtually independent of the fitting scheme used (Tabs. 20 and 21), confirming the reliability of the proposed method.

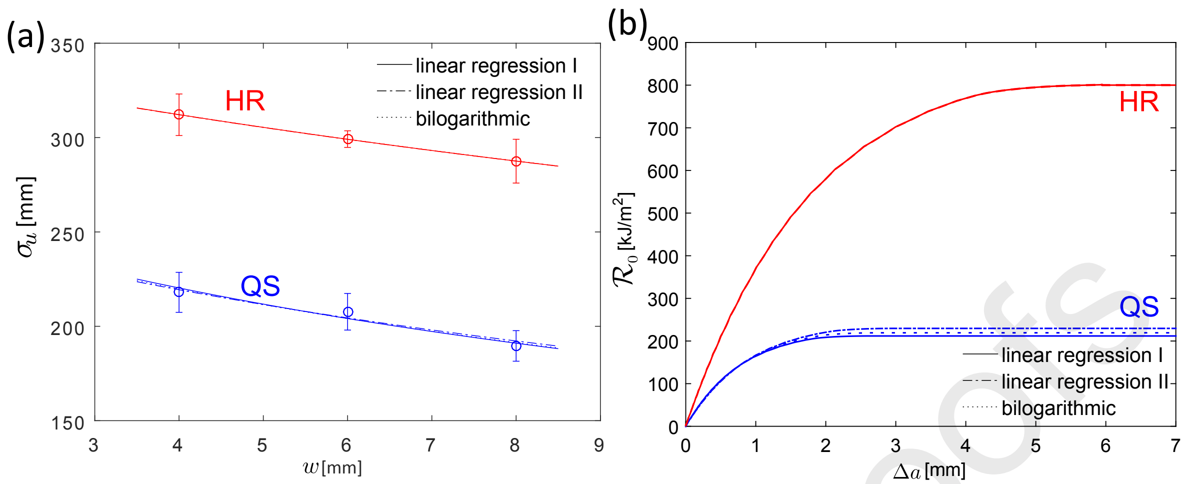

Figure 29: (a) Size effect law and (b) R-curves for QS and HR loading in tension.

Table 20: Summary of the fracture toughness properties for longitudinal tensile failure.

Regression fit	Property	QS	HR
Linear regression I	R_0^{ss} [kJ/m^2]	211.8	799.5
	l_{fpz} [mm]	2.61	5.95
Linear regression II	R_0^{ss} [kJ/m^2]	229.6	800.7
	l_{fpz} [mm]	2.99	5.96
Bilogarithmic	R_0^{ss} [kJ/m^2]	219.3	800.1
	l_{fpz} [mm]	2.77	5.95

Table 21: Coefficient for the analytical expression of the R-curve in tension.

Regression fit	Fitting parameter	QS	HR
Linear regression I	β [mm^{-1}]	0.2793	0.1228
	n [-]	4.656	4.648
Linear regression II	β [mm^{-1}]	0.2444	0.1226
	n [-]	4.651	4.648
Bilogarithmic	β [mm^{-1}]	0.2638	0.1228
	n [-]	4.650	4.648

4. Conclusions

A thorough methodology for the characterisation of GFRPs, with particular focus on the intralaminar fracture toughness for longitudinal tension and compression failure, has been developed. The analysis scheme used, based on the size effect method, requires the knowledge of the elastic parameters of the laminate that were determined by testing unnotched specimens in tension, compression, and shear, at quasi-static and dynamic strain rates. It was found that:

- In longitudinal compression, the Young's modulus increase with the strain rate (about 15% at 125 s^{-1}).
- In longitudinal tension the modulus was virtually strain rate insensitive, and this was found to be in good agreement with data reported for similar material systems.
- A slight strain rate effect was observed for the shear modulus, that was found to decrease by about 4%.

After the preliminary material characterisation, geometrically scaled notched specimens were tested at quasi-static and dynamic strain rates, and the nominal peak stress was found as a function of the characteristic size. This enabled the determination of the size effect law, and consequently of the intralaminar fracture toughness. Summarising:

- The intralaminar fracture toughness in longitudinal compression (associated with the propagation of a kink-band) was found to be strain rate dependent. The steady state value, $\mathcal{R}_{ss}$, was found to increase by about 114 %, while the length of the fracture process zone, l_{fpz}, increased by about 44 %.
- The increase of the intralaminar fracture toughness was also observed for longitudinal tension (about 280 %). An increase of the length of fracture process zone for longitudinal tension failure was also reported (about 120 %).
- The results were found to be independent on the function used to fit the size effect data.

As a concluding remark, it should be noted that the photo-mechanical configuration used (ie. SHPB, SHTB, DIC, and high-speed camera) set a benchmark for the experimental characterisation of FRPs at high strain rates.

Data availability

The raw/processed data required to reproduce these findings cannot be shared at this time due to technical or time limitations.

References

[1] R .L. Sierakowski. Strain rate effects in composites. *Applied Mechanics Reviews*, 50:741–761, 1997.

[2] G. C. Jacob, J. M. Starbuck, J. F. Fellers, S. Simunovic, and R. G. Boeman. Strain rate effects on the mechanical properties of polymer composite materials. *Journal of Applied Polymer Science*, 94:296–301, 2004.

[3] Vivekendra Singh. Literature survey of strain rate effects on composites. Technical Report TR18-001, RISE Research Institutes of Sweden, 07 2019.

[4] G. C. Jacob, J. M. Starbuck, J. F. Fellers, S. Simunovic, and R. Boeman. The effect of loading rate on the fracture toughness of fiber reinforced polymer composites. *Journal of Applied Polymer Science*, 96:899–904, 2005.

[5] C. McCarroll. *High rate fracture toughness measurements of laminated composites.* PhD thesis, Imperial College London, 2011.

[6] P. Kuhn, G. Catalanotti, J. Xavier, P.P. Camanho, and H. Koerber. Fracture toughness and crack resistance curves for fiber compressive failure mode in polymer composites under high rate loading. *Composite Structures*, 182:164 – 175, 2017.

[7] P. Kuhn, G. Catalanotti, J. Xavier, M. Ploeckl, and H. Koerber. Determination of the crack resistance curve for intralaminar fiber tensile failure mode in polymer composites under high rate loading. *Composite Structures*, 204:276 – 287, 2018.

[8] B. M. Leite, L. F. M. Leite, V. L. Reis, M. V. Donadon, and N. N. Alves da Silveira. Strain rate effects on the intralaminar fracture toughness of composite laminates subjected to compressive load. *Composite Structures*, 186:94–105, 2018.

[9] G. Catalanotti, J. Xavier, and P. P. Camanho. Measurement of the compressive crack resistance curve of composites using the size effect law. *Composites: Part A*, 56:300–307, 2014.

[10] G. Catalanotti, A. Arteiro, M. Hayati, and P. P. Camanho. Determination of the mode I crack resistance curve of polymer composites using the size-effect law. *Engineering Fracture Mechanics*, 118:49–65, 2014.

[11] G. Catalanotti and J. Xavier. Measurement of the mode II intralaminar fracture toughness and R-curve of polymer composites using a modified Iosipescu specimen and the size effect law. *Engineering Fracture Mechanics*, 138:202–214, 2015.

[12] R .F. Pinto, G. Catalanotti, and P. P. Camanho. Measuring the intralaminar crack resistance curve of fibre reinforced composites at extreme temperatures. *Composites: Part A*, 91:145–155, 2016.

[13] D. Dalli, G. Catalanotti, L.F. Varandas, B.G. Falzon, and S. Foster. Mode i intralaminar fracture

toughness of 2d woven carbon fibre reinforced composites: A comparison of stable and unstable crack propagation techniques. *Engineering Fracture Mechanics*, 214:427 – 448, 2019.

[14] H. Koerber, J. Xavier, and P. P. Camanho. High strain rate characterisation of unidirectional carbon-epoxy IM7-8552 in transverse compression and in-plane shear using digital image correlation. *Mechanics of Materials*, 42:1004–1019, 2010.

[15] H. Koerber. *Mechanical response of advanced composites under high strain rates*. PhD thesis, University of Porto, 2010.

[16] R. Gerlach, C. Kettenbeil, and N. Petrinic. A new split Hopkinson tensile bar design. *International Journal of Impact Engineering*, 50:63–67, 2012.

[17] H. Koerber and P. P. Camanho. High strain rate characterisation of unidirectional carbon-epoxy IM7-8552 in longitudinal compression. *Composites Part A*, 42:462–470, 2011.

[18] S. Nemat-Nasser, J. B. Isaacs, and J. E. Starrett. Hopkinson techniques for dynamic recovery experiments. *Proceedings: Mathematical and Physical Sciences*, 435:371–391, 1991.

[19] H. Kolsky. An investigation of the mechanical properties of materials at very high rates of loading. *Proc. Phys. Soc. London*, Sect. B. 62 (II-B):676–700, 1949.

[20] G. T. Gray III. *Classic split-Hopkinson pressure bar testing. In: ASM handbook mechanical testing and evaluation*, volume 8. ASM International Ohio USA, 2000, pp. 462-476.

[21] J.L. Pereira, J. Xavier, B. Ghiassi, J. Lousada, and J. Morais. On the identification of earlywood and latewood radial elastic modulus of pinus pinaster by digital image correlation: A parametric analysis. *The Journal of Strain Analysis for Engineering Design*, 53(8):566–574, 2018.

[22] DIN EN ISO 14129, Fibre-reinforced plastic composites - Determination of the in-plane shear stress/shear strain response, including the in-plane shear modulus and strength, by the pm45 tension test method; German version EN ISO 14129:1997, 1998.

[23] F. Jiang and K. S. Vecchio. Hopkinson bar loaded fracture experimental technique: A critical review of dynamic fracture toughness tests. *Applied Mechanics Reviews*, 62:1–39, 2009.

[24] Z. Suo, G. Bao, B. Fan, and T. C. Wang. Orthotropy rescaling and implications for fracture in composites. *International Journal of Solids and Structures*, 28:235–248, 1990.

[25] G. Bao, S. Ho, Z. Suo, and B. Fan. The role of material orthotropy in fracture specimens for composites. *International Journal of Solids and Structures*, 29:1105–1116, 1992.

[26] Z. P. Bažant and J. Planas. *Fracture and size effect in concrete and other quasibrittle materials*. CRC Press LLC, Boca Raton, Florida, USA, 1998.

[27] M. Ploeckl, P. Kuhn, J. Grosser, M. Wolfahrt, and H. Koerber. A dynamic test methodology for analyzing the strain-rate effect on the longitudinal compressive behavior of fiber-reinforced composites. *Composite Structures*, 180:429–438, 2017.

[28] M. M. Shokrieh and M. Omidi. Compressive response of glass-fiber reinforced polymeric composites to increasing compressive strain rates. *Composite Structures*, 89:517–523, 2009.

[29] P. Kumar, A. Garg, and B. D. Agarwal. Dynamic compressive Behavior of unidirectional GFRP for various fibre orientations. *Materials Letters*, 4:111–116, 1986.

[30] D. Lee, T. S. Tim, and S. S. Cheon. Impact energy absorption characteristics of composite structures. *Composite Structures*, 50:381–390, 2000.

[31] Z. Whu, A. Gunnion, R. S. Thomson, P. Kuhn, H. Koerber, and C. Song. High strain rate testing of glass-epoxy and hybrid laminates. In *The 2nd China International Congress on Composite Materials, Zhenjiang, China, 2015*, 2015.

[32] H. Koerber. Test Evaluation Report and Dynamic Material Property Database. Technical Report Deliverable D3.2, Clean Sky 2, Project DeMAnD, December 2018.

[33] D. F. Adams and C. G. Adams. Tensile Impact Tests of AS4/3501-6 and S2/3501-6 Unidirectional Composites and 3501-6 Epoxy Matrix. *Journal of Composite Materials*, 24:256–268, 1990.

[34] M. M. Shokrieh and M. J Omidi. Tension behavior of unidirectional glass/epoxy composites under different strain rates. *Composite Structures*, 88:595–601, 2009.

[35] R. Gerlach, C. R. Siviour, J. Wiegand, and N. Petrinic. The Strain Rate Dependent Material Behavior of S-GFRP Extracted from GLARE. *Mechanics of Advanced Materials and Structures*, 20:505–514, 2013.

[36] M. M. Shokrieh and M. J. Omidi. Investigation of strain rate effets on in-plane shear properties of glass/epoxy composites. *Composite Structures*, 91:95–102, 2009.

[37] J. L. Tsai and C. T. Sun. Strain rate effect on in-plane shear strength of unidirectional polymeric composites. *Composite Science and Technology*, 65:1941–1947, 2005.